Mixed Compressive Sensing Back-Projection for SAR Focusing on Geocoded Grid

Adrian Focsa ⬤, *Student Member, IEEE*, Andrei Anghel ⬤, *Senior Member, IEEE*, Mihai Datcu ⬤, *Fellow, IEEE*, and Stefan-Adrian Toma

Abstract—**This article presents a new scheme called 2-D mixed compressive sensing back-projection (CS-BP-2D), for synthetic aperture radar (SAR) imaging on a geocoded grid, in a single measurement vector frame. The back-projection linear operator is derived in matrix form and a patched-based approach is proposed for reducing the dimensions of the dictionary. Spatial compressibility of the radar image is exploited by constructing the sparsity basis using the back-projection focusing framework and fast solving the reconstruction problem through the orthogonal matching pursuit algorithm. An artifact reduction filter inspired by the synthetic point spread function is used in postprocessing. The results are validated for simulated and real-world SAR data. Sentinel-1 C-band raw data in both monostatic and space-borne transmitter/stationary receiver bistatic configurations are tested. We show that CS-BP-2D can focus both monostatic and bistatic SAR images, using fewer measurements than the classical approach, while preserving the amplitude, the phase, and the position of the targets. Furthermore, the SAR image quality is enhanced and also the storage burden is reduced by storing only the recovered complex-valued points and their corresponding locations.**

Index Terms—**Back-projection, bistatic, compressive sensing (CS), focusing, synthetic aperture radar (SAR).**

I. INTRODUCTION

SYNTHETIC aperture radar (SAR) imaging is a powerful technique for direct or indirect measurements of physical parameters characterizing the illuminated scene, capable of collecting day-and-night, all-weather data. Recent requirements of shorter repeat-pass time, wider swath coverage and increased resolution push the limits of storage and computational hardware. As conventional imaging procedures deal with large amounts of data acquired under the Nyquist–Shannon theorem

limit, the relatively new theory of compressive sensing (CS) comes with an efficient solution mainly based on the idea of sparsity. The method shows great potential, being used for synthetic aperture radar (SAR) image focusing [1]–[7], inverse SAR image reconstruction [8]–[11] noise radar imaging [12], tomographic [13], [14] interferometric applications [15], [16], [17]. CS methods were also successfully employed in through-the-Wall radar imaging [18], [19].

The CS paradigm [20], [21] involves the direct acquisition of data in a compressed form together with accurate information reconstruction from fewer samples than imposed by Nyquist–Shannon lower bound. Hence, CS is concerned about information preservation by discarding redundant raw data over the acquisition. The goal of the CS techniques is to decrease the number of acquired samples of a signal relying on the existence of a set of basis vectors, where raw data has a sparse representation. The main shortcomings related to CS techniques are listed in the following: finding a sparsity basis, estimating the degree of sparsity, choosing the appropriate recovery algorithm, evaluating the quality of the reconstruction, lowering the produced artifacts, and reducing the computational complexity.

So far, many proposed methods have tried to solve one or more of the abovementioned issues by dividing the SAR image formation problem into two or more subprocesses (range compression, range cell migration correction, residual correction, and azimuth compression). The Matched filter [1], [2], the Range–Doppler [22] or the Chirp-Scaling [3] and $\omega - k$ SAR image formation algorithms inspired CS-based frameworks for generating high-quality images, while, at the same time, decreasing the amount of stored data. The most common assumption in CS-based SAR imaging is the spatial sparsity [23]. In [24] and [25], the problem of low spatial sparsity is addressed introducing low-rankness hypothesis regarding the nonsparse scenes, whereas in [26] the magnitude sparseness in the Wavelet domain is harnessed. Nevertheless, such approaches are computationally expensive. The effectiveness of the CS-greedy solvers for such low-sparse areas is limited. Yet, the computational complexity for SAR imaging–large scale problem also restricts the involvement of Basis Pursuit CS-solvers [27].

Recently, the demand for efficient time-domain algorithms for SAR image formation has increased. Therefore, we chose to exploit the advantages of the well-known back-projection (BP) [28], [29] algorithm. Apart from its ability to process geocoded grids for both monostatic and multistatic geometries, BP provides robustness concerning specific SAR space-variant
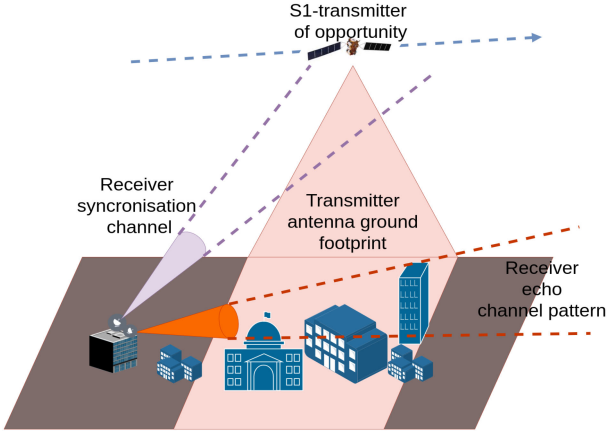
Fig. 1. Bistatic scenario: Sentinel 1 (Tx)-COBIS (Rx).

effects and as demonstrated in [30], it is more suitable for future space-borne SAR missions than frequency domain focusing algorithms.

This article introduces a combined CS-BP SAR imaging framework called CS-BP-2D for a user-defined grid, which manages to discard raw data while preserving the magnitude and the phase of the SAR image. It exploits the spatial sparsity property [11] characterizing some urban areas and bistatic scenarios (as sketched in Fig. 1). We derive the sparsity basis inspired by the BP focusing framework. Compared to the other CS-based techniques [1], [3] our approach does not need to decouple range and azimuth. Besides, CS-BP-2D has no need for range cell migration correction. The solver chosen for the CS problem is the orthogonal matching pursuit (OMP) reconstruction algorithm [31], as its performances regarding complexity, accuracy, and speed, make it suitable for large scale problems. The processing flow also includes a nonlinear filter that reduces the artifacts. It is based on SAR system point spread function (PSF). By decoupling range and azimuth processing, the error propagation is likely to occur. Hence, failure of range profile reconstruction will be intensified in the azimuth compression step. This motivates our proposed scheme to consider a single measurement vector approach. To lower the dimensions of the involved matrices (for extended scenes), CS-BP-2D splits the grid in patches and selects only the useful raw data. The SAR image is obtained after applying CS-BP-2D independently on each patch and merging the results.

The rest of this article is organized as following. Section II briefly reviews the BP algorithm. Section III presents an overview of the CS theory. The CS-BP-2D methodology is detailed in Section IV. Simulated and real-world data are employed in various focusing workflows. The results are presented and discussed in the Section V. Section VI concludes this article.

II. BP ALGORITHM

The main concerns regarding SAR image formation are related to the reconstruction accuracy and the computational burden. In order to accomplish these two requirements, the developed algorithms use particular assumptions such as linear trajectories for the SAR platform, geometric approximations,

and scene sparsity assumptions. Many of these limitations may lead to resolution degradation [32]. Our approach considers computing an independent focusing dictionary for each subimage rather than using approximations to transform a reference dictionary from one patch to another. The lack of generality is mentioned in [33], where authors state that the time domain BP algorithm may be a solution to avoid previously mentioned constraints. They also propose an improved version for bistatic SAR focusing called fast bistatic fast factorized BP based on SAR sub-aperture processing sped-up by the fast Fourier transform algorithm.

In [28] and [34], MATLAB implementations of BP are presented. Basically, BP involves the following processing steps.

A1. Apply a matched filter on every received signal (either in the time domain or in the frequency domain), generating the range-compressed signal.

A2. Linearly interpolate every range-compressed signal from step A1 on a predefined focusing grid.

A3. Sum up phase-corrected contributions of every range-compressed signal to each grid cell to generate the complex SAR image.

We chose BP because its steps may be easily adapted for parallel computing and provide invariance to the imaging mode. The main disadvantages are the computational expense and the precision requirements regarding the imaging geometry. Our main goal is to derive the BP linear operator, i.e., the system transformation matrix (**STM**) associated with the BP SAR image formation algorithm and to reduce its dimension through the patched-based processing.

III. CS KEY-POINTS

In this section, we describe the main key-points of applying CS to SAR imaging. CS is a technique that allows for the reconstruction of a signal from a smaller number of samples than the Nyquist limit, if the signal is sparse or compressible in a specific basis [20], [35]. Our framework considers the spatial sparsity of the scene, i.e., the BP focusing operator will act as a basis in which the representation of raw data will be sparse. For the 1-D chirp-based impulse radar signal reconstruction model, the received signal $s_r \in \mathbb{C}^N$ is sparse if there is a basis $\{\Psi_i\}, i = \overline{1, N}$, where s_r can be represented as the weighted sum of only $K \ll N$ basis vectors, as in (1), where θ_i are the weights of every basis vector in the linear combination of s_r, and the norm $||\theta||_0 = K$. In (1) the right side refers to those dictionary atoms with K biggest weights

$$s_r[n] = \sum_{i=1}^{N} \theta_i \Psi_i = \sum_{i=1}^{K} \theta_i \Psi_i \tag{1}$$

As shown in [1], the use of the matched filter linear operator for the reconstruction of range profiles from the under sampled version of $s_r[n]$ may work under some constraints: the scene contains only a few point scatterers (i.e., sparsity condition) and the signal-to-noise ratio (SNR) is large enough (i.e., noise-related condition). According to [20], CS is concerned about two matrices: the first one is the basis transform matrix, previously defined by Ψ_i vectors, and the second one is the measurement matrix
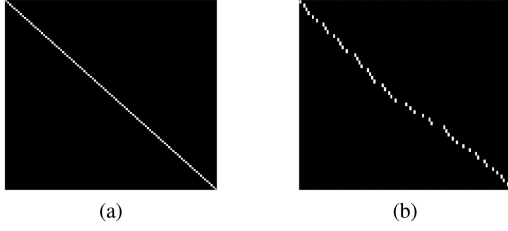
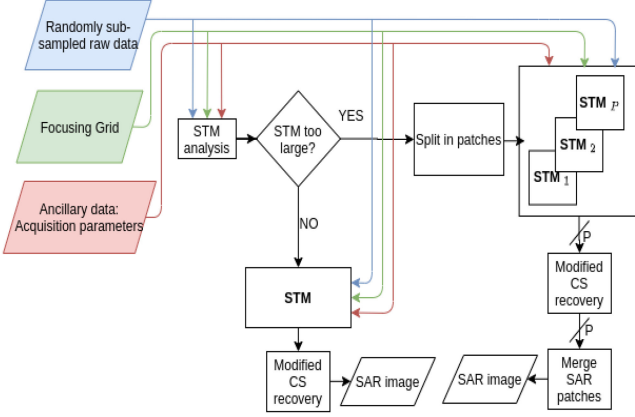Fig. 2. Sampling matrices in the context of SMV: (a) classic sampling matrix and (b) random sampling matrix.

Fig. 3. CS-BP-2D workflow.

$\mathbf{\Phi}$ (Fig. 2). In the classic acquisition, $\mathbf{\Phi}$ is the identity matrix, suggesting the uniform sampling process, Fig. 2(a), whereas a CS-specific random sampling matrix is shown in Fig. 2(b). The latter is employed in the proposed focusing scheme. In (2), measured samples $\mathbf{y} \in \mathbb{C}^M, M < N$ are expressed in a compact format, where $\boldsymbol{\theta}$ contains basis vector weights.

$$\mathbf{y} = \mathbf{\Phi}\mathbf{\Psi}\theta = \boldsymbol{\theta}s_r. \tag{2}$$

Basis matrix must respect the restricted isometry property (R.I.P) and the incoherency property. Intuitively, R.I.P. guarantees that the distances between points in the original space are preserved in the transformed space. If these two properties hold, CS theory proves that the signal can be exactly recovered [36]. A more detailed analysis of these properties will be made for the particularly used matrices in the following section. The SAR image formation is a large-scale problem, thus we chose to solve (2) by OMP. OMP is one of the simplest and fastest matching pursuit algorithms. The solution is computed using a constrained least-squares approximation (3).

$$\mathbf{x}_{\text{OMP}} = \min_{\mathbf{x}} ||\mathbf{y} - \mathbf{\Theta}\mathbf{x}||_2^2 \text{ s.t. } ||\mathbf{x}||_0 \leq K. \tag{3}$$

By solving (3), one may want to recover the following information about scatterers: the relative strengths, the positions in the SAR image, and the phase information.

IV. CS-BP-2D FRAMEWORK

The diagram in Fig. 3 illustrates the proposed workflow. Depending on the dimensions of the measurement matrix *STM*, the CS recovery algorithm may be applied either on patches or for the entire grid at once. For the latter, the modified OMP

algorithm outcomes are eventually assembled into the full SAR image.

The main contributions of the proposed processing chain are the following: 1) it is independent of the SAR scanning mode; 2) CS-BP-2D has no need for azimuth range decoupling; 3) it assures a straightforward accommodation for monostatic and bistatic acquisition scenarios; and 4) provides a modified CS solver, which involves the system's PSF for artifact suppression. Also, the PSF-based filter accounts for the grid mismatch errors. The proposed processing is flexible concerning the input data. CS-BP-2D may be applied directly on range compressed data.

The following sections will discuss the design of the STM, the modified greedy approach employed for CS recovery, which includes an artifact rejection filter. Also, an analysis of the sparsity degree (K) estimation is carried out.

A. Sparsifying Dictionary Design

The matrices associated with BP processing steps are denoted as follows: *matched filter matrix (MFM)*, *grid interpolation matrix (GIM)* and *azimuth summation matrix (ASM)*. We need to build these three matrices before generating the STM. Intuitively, *STM* simultaneously achieves two types of compression: range compression and azimuth compression with no need for range cell migration correction.

The proposed process flow employs a single measurement vector (SVM) approach. Hence, azimuth measurements $\mathbf{s}_r^p, p = \overline{1, N_p}$ are first concatenated into a column vector. Suprascript index p suggests the azimuth scan position

$$\mathbf{s}_{mf}[n] = \mathbf{MFM} \times \mathbf{vec}\left(\mathbf{s_r^P}[\mathbf{n}]\right), n = \overline{1, N}. \tag{4}$$

The matched filter operation, as suggested in (4) is performed by projecting the acquired samples onto the line vectors of *MFM* matrix. The vec() operator transforms an $N \times N_P$ matrix in a $NN_P \times 1$ column vector. Every row vector of *MFM* is a complex conjugated time shifted version of the transmitted signal $\mathbf{s}_t^p[n]$. The relative time shift between two consecutive lines is equal to the sampling interval. The second processing step in BP is the linear interpolation. In our framework, it is accomplished by *GIM*. To design *GIM*, first, the Euclidean distances from the transmitter-Tx to each grid cell and from each grid cell to the receiver-Rx are calculated using (5). Subscript indices i and j refer to the position of the cell in the predefined grid. The positions of the transmitter $(x_{Tx}^p, y_{Tx}^p, z_{Tx}^p)$, receiver $(x_{Rx}^p, y_{Rx}^p, z_{Rx}^p,)$ and grid cells (x_{ij}, y_{ij}, z_{ij}) for each transmitted pulse p should be precisely known

$$d_{ij}^p = \sqrt[2]{(x_{Tx}^p - x_{ij})^2 + (y_{Tx}^p - y_{ij})^2 + (z_{Tx}^p - z_{ij})^2}$$
$$+ \sqrt[2]{(x_{Rx}^p - x_{ij})^2 + (y_{Rx}^p - y_{ij})^2 + (z_{Rx}^p - z_{ij})^2}. \tag{5}$$

Only useful samples in $[R_{\min}, R_{\max}]$ interval are selected for the design of the *STM*. This selection process contributes to the lowering of the matrix dimensions

$$R_{\min} = \min\left(d_{ij}\right)$$
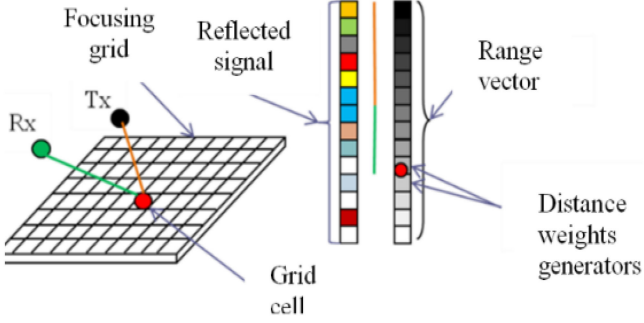$$R_{\max} = \max\left(d_{ij}\right) \tag{6}$$

Fig. 4.   GIM formation–bistatic scenario.

The closest two samples in each range profile, which may come from a specific grid cell are obtained by minimizing the absolute difference between the range distance vector $\mathbf{r_{vec}}$ and Tx-grid cell-Rx distance matrix

$$\tilde{k}_{1,2} = \min_{k} |\mathbf{r_{vec}}[k] - d_{ij}^{p}|. \tag{7}$$

The range vector $\mathbf{r_{vec}}$ is defined using (8). In (8), c denotes the wave propagation speed. This vector contains distances in the range interval $[R_{\min}, R_{\max}]$ with an increment computed as the distance traveled by the electromagnetic wave in half of the sampling interval $1/F_s$. The determination of the interpolation weights is sketched in Fig. 4.

$$\mathbf{r_{vec}}[k] = k\frac{c}{2F_s}, k = \overline{0, N-1}. \tag{8}$$

The range vector is represented using gray-scale samples (where the intensity increases with the distance), whereas the corresponding recorded samples values are illustrated by random colors.

Once the indexes $\tilde{k}_{1,2}$ are determined, the *GIM* may be constructed. As linear interpolation is used, every line of GIM contains two nonzero elements. The resulted interpolated values $\mathbf{s}_{\text{interp}}^{p}[d_{ij}^{p}]$ corresponding to d_{ij} grid cell at pulse p are computed using (9).

$$\mathbf{s}_{\text{interp}}^{p}[d_{ij}^{p}] = \sum_{l=1}^{2} 2\mathbf{s}_{mf}^{p}[\tilde{k}_{l}]\frac{|\mathbf{r_{vec}}[\tilde{k}_{l}] - d_{ij}^{p}|F_s}{c} \tag{9}$$

The last step is the design of the *ASM*. It performs the summation of every pulse contribution and the compensation of the phase component caused by the distance Tx-grid cell-Rx. In other words, the azimuth compression is achieved through *ASM* multiplication. This step is synthesized by (10). The SAR focused image is achieved by multiplying previously interpolated samples with *ASM* and reshaping the outcome in compliance with the grid size.

$$\mathbf{I_{SAR}}(i,j) = \sum_{p=1}^{N_p} \mathbf{s}_{\text{interp}}^{p}[d_{ij}^{p}]e^{\frac{-2\pi F_c d_{ij}^{p}}{c}}. \tag{10}$$

Every *ASM* line will have only N_p nonzero elements and guarantees that row vectors are orthogonal. If we consider N_x and N_y the dimensions of the focusing grid, the resulted *ASM* will have $N_x \times N_y$ lines and $N_x \times N_y \times N_p$ columns. The sparseness of *ASM* is sketched in Fig. 5. Even though the *ASM* dimensions
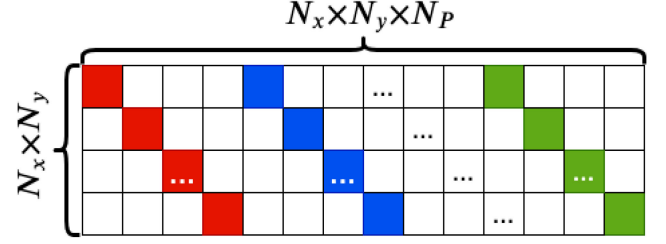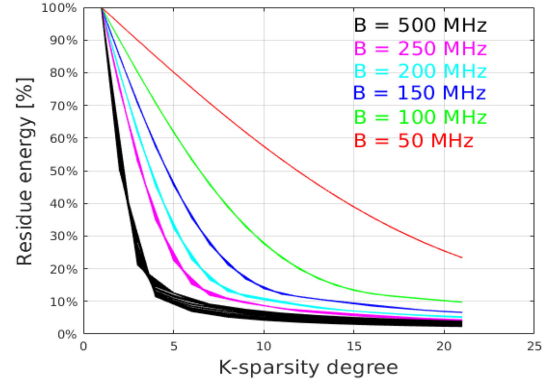

Fig. 5.   ASM general form.

Fig. 6.   Residue energy variation by changing the bandwidth of the transmitted signal.

increases, it is worth noticing that most of the values are null and only $N_x \times N_y \times N_p$ are nonzero values.

$$STM = ASM \times GIM \times MFM. \tag{11}$$

Finally, the overall BP complex-valued operator *STM,* which will be our $\boldsymbol{\Psi}$ matrix in the CS frame is derived using (11). As an alternative for (10), the SAR focusing may be simply accomplished by multiplying *STM* with the vectorized form of the received signals. The *STM* operator is the matched filter adapted for the specified focusing grid. The energy of a scatterer, initially spread on both range and cross-range in the raw data may be now focused on both directions using *STM*.

B. CS Recovery Aspects

The reconstruction quality guaranteed by CS theory is achieved only if the sparsifying dictionary exists and the sensing matrix $\boldsymbol{\Theta}$ satisfies the incoherency property and the R.I.P. Since the proposed method implies Gaussian randomly subsampling, as proved in [37], the incoherence holds. Also, the amount of discarded data should vary inversely proportional to the data sparsity and SNR. Moreover, the R.I.P. holds because *STM* contains the matched filter coefficients for a linear frequency modulated pulse in both range and azimuth directions.

We used OMP (a greedy solver) for the SAR imaging problem. The only parameter to be set is the sparsity degree of the scene, i.e., K. It may be easily estimated from a single range profile per aperture by thresholding the residue energy in the OMP computing flow. However, the adopted threshold should be modified according to the bandwidth of the transmitted signal and the azimuth chirp bandwidth. In Fig. 6, simulated
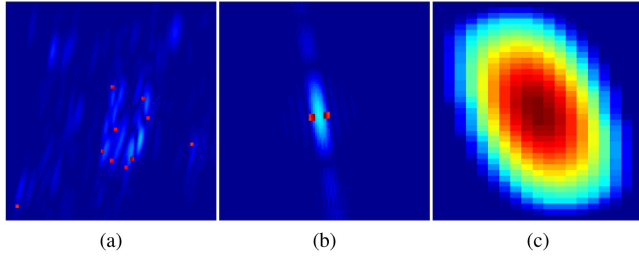
Fig. 7. Erroneous reconstructed points (red dots) examples in bistatic (a) and monostatic (b) scenarios with oversampled focusing grids, and (c) simulated PSF - main lobe.

SAR data were used to determine the variation of the residue energy sweeping both bandwidth and K. For each bandwidth, 100 azimuth measurements were analyzed. The pixel spacing was chosen three times smaller than the range resolution cell corresponding to each bandwidth.

It is important to notice that the bigger the bandwidth B the steepest the gradient in the residue energy. Specifically, the small pulse generated by the autocorrelation hidden in the *STM* operator converges to a Dirac delta function and the spatial sparsity assumption is better sustained. In the experimental section, a coarse value for K is obtained by thresholding the residue energy slope.

Considering the same K estimate for many azimuth measurements has the same motivation as the use of multiple measurement vectors in 2-D problems [38], i.e., the information in raw/range-compressed data matrix is structured. Therefore, during small illumination intervals, the range migration may be neglected and the spread of a single target on the cross-range direction share the same bin. Even so, erroneously reconstructed pixels are produced in the SAR image. We have identified a systematic source of error in the OMPs correlation computation. Because complex-valued vectors are employed, the decision to select dictionary atoms from $\boldsymbol{\Psi}$ is taken based on the magnitudes of the correlation coefficients. Hence positive correlations cannot be distinguished between negative correlations. Also, the grid mismatch may cause similar behavior. In this regard, a local synthetic point spread (PSF) function-based postprocessing filter is designed. It is motivated by the fact that negative correlations are more likely to be located on the first null vicinity of the strong point-like targets or in regions, where the magnitude of the gradient in the detected image (magnitude of the complex-valued pixels) is comparable to the highest gradient of the main lobe of the PSF. In Fig. 7(a) and (b) most erroneous pixels locations are highlighted for monostatic and bistatic setups. In Fig. 7(c), a simulated PSF-based kernel is illustrated.

The use of the proposed filter makes K estimate precision requirement decrease. In this regard, K is artificially overestimated. By choosing a sparsity degree bigger than needed, weak target detection is improved. The implementation of the filter comprises the following steps:

Step 1: Sort reconstructed points (not null) in x_{OMP} in the descending order of their magnitude.

Step 2: Center the PSF kernel on the location of previously sorted values starting with the one characterized by the biggest magnitude.

Step 3: Discard pixels located in the neighborhood of the border of the PSF main lobe.

Step 4: Update the estimated points using (12).

$$\boldsymbol{x}_{CS-BP-2D} = \left(\boldsymbol{\Theta}_{\text{filtered}}^T \boldsymbol{\Theta}_{\text{filtered}} \right)^{-1} \boldsymbol{\Theta}_{\text{filtered}}^T \boldsymbol{y}. \qquad (12)$$

The third step implies that some pixels become null during the filter iterations. Hence, they are not considered for the filtering procedure. In (12), $\boldsymbol{\Theta}_{\text{filtered}}$ contains the atoms given by the nonrejected recovered points by conventional OMP. By ignoring the points that are likely to be artifacts, the new solution is refined. In the next section conventional OMP simply refers to using the *STM* as sparsifying basis, but as opposed to CS-BP-2D, it does not employ the postprocessing filter.

C. Computational Complexity

CS-BP-2D achieves a computational complexity having the same order as the conventional algorithm used for focusing i.e., BP. Recent papers addressing SAR imaging by CS-means also report computational complexities similar to the ones obtained by the classic approaches [23], [26]. The computational load is dictated by the interpolation block (*GIM*). However, considering the SAR image formation of BP through $STM \times \boldsymbol{vec}(\boldsymbol{s}_r^p[n])$, the complexity is $\mathcal{O}(n^3)$. CS-BP-2D computational burden is strictly given by the recovery algorithm. For high sparse scenes, OMP complexity is dominated by the projection of the residual vector onto the sparsifying basis. The resulted complexity is $\mathcal{O}(\text{mnk})$, with m being the number of measured samples, n - the number of samples in the recovered signal and k-the sparsity degree. Thus, CS-BP-2D is suitable for sparse scenes, where $mk \ll n^2$.

D. Discussion

The recovery performance achieved by CS-BP-2D depends on the CS solver robustness regarding the dictionary redundancy, the sparsity degree, and the sparsity—undersampling tradeoff. In addition, as demonstrated through [39, Th. 4], in general, the greedy solvers do not ensure denoising. Hence, the success rate in noisy conditions (white Gaussian noise) depends on $\min(\boldsymbol{x}_0)$, $\max(\boldsymbol{x}_0)$, noise power (σ^2), and the properties of the sensing matrix (the coherence limits of $\boldsymbol{\Theta}$). Intuitively, since the atoms selection from $\boldsymbol{\Theta}$ is achieved by means of correlation, the smallest nonzero coefficient in the "oracle" estimator ($\boldsymbol{x}_0$) has to be greater than the noise power. OMP reaches a reasonable phase recovery assuming a relatively high level of sparsity and mild noise conditions. Yet, in noisy scenarios and for fine grid spacing the inflation of the dictionary atoms correlation lower CS-BP-2D framework performance. Therefore, more advanced CS greedy solvers such as ROMP [40], GOMP [41], or CMP [42] may be employed. We have empirically determined that the optimal grid spacing should be between one third and one half of the smallest spatial resolution (range and azimuth). A coarser grid spacing would increase the off-grid errors, whereas a finer spacing grid

TABLE I
EXPERIMENTAL PARAMETERS FOR SIMULATED DATA

Parameter	Value
Carrier frequency F_c	5.405 GHz
Bandwidth / Range resolution	50 MHz / 3m
Sampling frequency F_s	150 MHz / 100 MHz
Pixel size	1 m / 0.5 m / 3 m
Aperture length / Azimuth resolution	10 m / 2.775 m
Range to mid swath	1000 m

TABLE II
RESULTS ON SIMULATED DATA CONTAINING THREE POINT-LIKE TARGETS

	$SNR = \infty$ 25% of raw data		$SNR = -6dB$ 50% of raw data	
	MAE phase[deg]	RMSE amplitude	MAE phase[deg]	RMSE amplitude
BP	-	9.2513e-05	-	**3.3639e-04**
CS-BP (without filter)	2.5843	1.2459e-04	2.6309	6.6063e-04
CS-BP-2D	**0.7411**	**2.3172e-05**	1.4343	5.2556e-04

not only would boost the dimensionality of the problem but also would violate the RIP.

V. EXPERIMENTS AND VALIDATION

A. Simulated Data

First, we use simulated raw data to prove CS-BP-2D framework effectiveness. The magnitude and the phase of the resulted SAR images are confronted with the ones achieved by conventional CS-BP (without PSF-based filter) and by BP. We have carried out five experiments illustrating the behavior of the proposed processing-flow.

The additive white Gaussian noise considered in the following experiments was introduced in the raw data. The SNR was computed using (13). In (13), σ denotes the noise standard deviation, whereas N represents the number of samples of the signal to be reconstructed

$$\text{SNR} = 10\log\frac{||x||_2^2}{N\sigma^2}[\text{dB}]. \tag{13}$$

In the first experiment, simulated raw data is produced in a monostatic configuration, where the illuminated sparse scene (30 × 30 m) contains three-point scatterers with different normalized magnitudes: 0.75, 0.4, and 1. The transceiver has a linear trajectory along the *y*-axis (cross-range direction). The length of the synthesized aperture is 10 m. Every 0.3 m a range profile is recorded. The parameters of the experimental setup are listed in Table I. Remarkably, 75% of the samples in raw data were discarded in the ideal (SNR = ∞) setup. The second configuration implies a nosy acquisition. Thus, only 50% randomly selected samples were dropped out. The imaging results presented in Fig. 8 show that CS-BP-2D is able to detect and localize scatterers not only in ideal conditions, Fig. 8(d), but also in noisy environments, Fig. 8(g). For visual comparison, Fig. 8(a) illustrates the ideal SAR image. The SAR images processed by BP are displayed in Fig. 8(b) and (e). In addition, the raw outcomes of CS-BP (without filter) are also presented for comparison in Fig. 8(c) and in Fig. 8(f). Table II proves that CS-BP-2D provides accurate results in terms of phase and
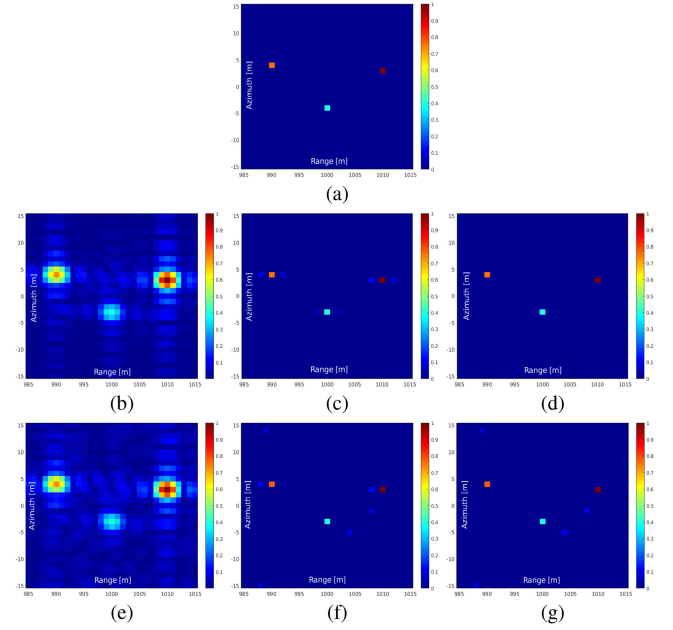

Fig. 8. SAR imaging results for the first experiment with simulated raw data: (a) Ideal point scatterer image, (b) BP- SAR image (no noise), (c) SAR image (no noise) obtained by CS-BP (without filter), (d) CS-BP-2D outcome(no noise) (e) BP-SAR image with SNR = −6dB (f) SAR image obtained by CS-BP(without filter) with SNR = −6dB and (g) CS-BP-2D SAR image with SNR = −6dB
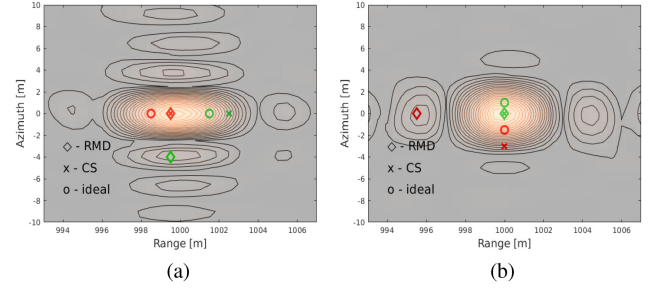

Fig. 9. Super-resolution testing in target detection experiment with simulated data for: (a) range resolution and (b) azimuth resolution.

magnitude. For the phase component, the mean absolute error (MAE) relative to BP outcome was computed. The amplitude recovery performance is indicated by root mean square error (RMSE). It was evaluated relative to the ideal magnitudes of the simulated scatterers ([0.75, 0.40, 1.00]). CS-BP-2D outperforms both BP and CS-BP (without filter) for SNR = ∞. For the second scenario, SNR = −6dB (on raw data), CS-BP-2D still provides a better phase estimate than CS-BP. Also, the recovered amplitudes are closer to the ones obtained by conventional BP. The quality parameters reported in Table II were obtained by averaging the results over 100 iterations.

Due to the simultaneous involvement of azimuth and range bandwidth, super-resolution may be achieved. In Fig. 9, two sets of point-like targets are located under the resolution limit in range Fig. 9(a) and in azimuth Fig 9(b). Their corresponding coordinates are: [998.4, 0, 0], [1001.3, 0, 0] and [1000, -1.35, 0], [1000, 1.25, 0], respectively. CS-BP-2D outcome offers a better estimate for the positions of the targets than regional maxima detector (RMD) even though only 20% randomly selected raw
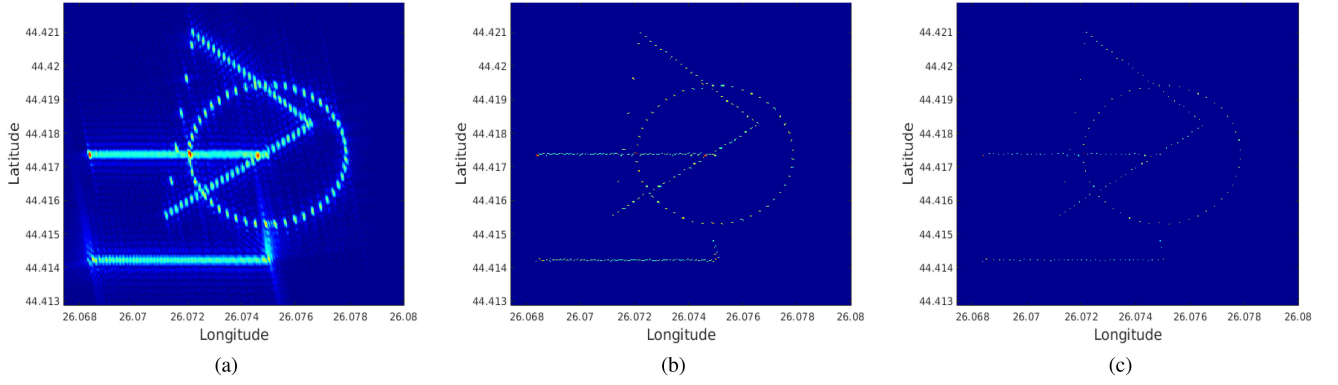
Fig. 10. SAR images obtained in the third experiment where Sentinel 1 emulated data is involved (a) BP, (b) CS-BP (without filter), and (c) CS-BP-2D.
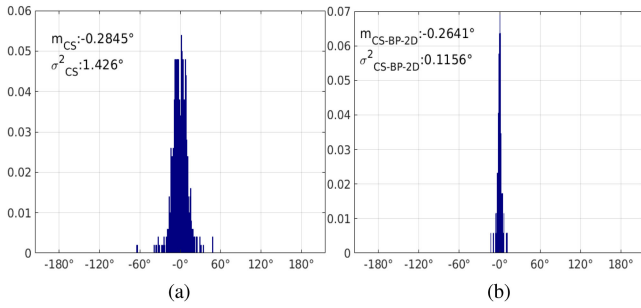

Fig. 11. Relative phase error probability density function for: (a) CS-BP(without filter) and (b) CS-BP-2D. The estimated phase error was performed for the images in Fig. 10.

Fig. 12. MAE of the phase: (a) No data discarded and (b) 25% of data discarded.

data were used for reconstruction. RMD uses the intensity gradients relative to the eight pixels in the 3×3 neighborhood to determine if the current pixel is a local maximum.

The third experiment emulates the Sentinel 1 acquisition process. A focusing grid of 1000×1000 m and a pixel size of 3 m are considered. The geographical coordinates of the grid center are [44.417443N, 26.073496E] (Vulcan Value Center, Bucharest, Romania).

The BP outcome in Fig. 10(a) is put in contrast with conventional CS-BP(without filter)—Fig. 10(b) and with CS-BP-2D - Fig. 10(c) in terms of magnitude. After the proposed nonlinear filter is applied, most of the erroneous reconstructed points were removed. The relative phase errors obtained by CS-BP (without filter) recovery and our method are displayed in Fig. 11. CS-BP-2D outperforms classic CS reconstruction, having a phase error variance more than 10 times smaller.

Furthermore we have assessed the performance of CS-BP-2D by varying the SNR and the sparsity of the region of interest. First, we have considered a sparse scene containing three-point scatterers. Then, we have varied the SNR of the raw data in the interval $[-18, -4]$ dB. The reconstruction accuracy have been measured in terms of MAE computed for the phase component. The results presented in Fig. 12 show that CS-BP-2D provides the same phases as the BP when the raw data is not randomly down-sampled, Fig. 12(a). In Fig. 12(b), it is remarkable that for the entire range of the SNRs, our method provides smaller phase errors than CS-BP(without filter) with only 75% of data.
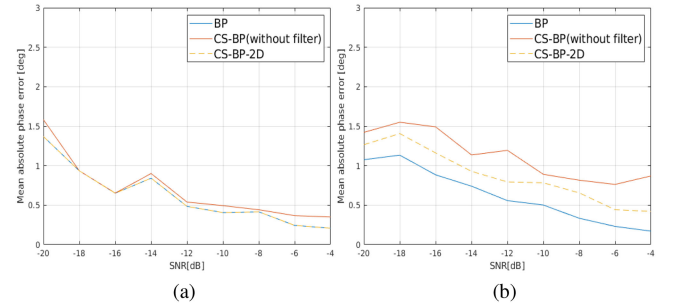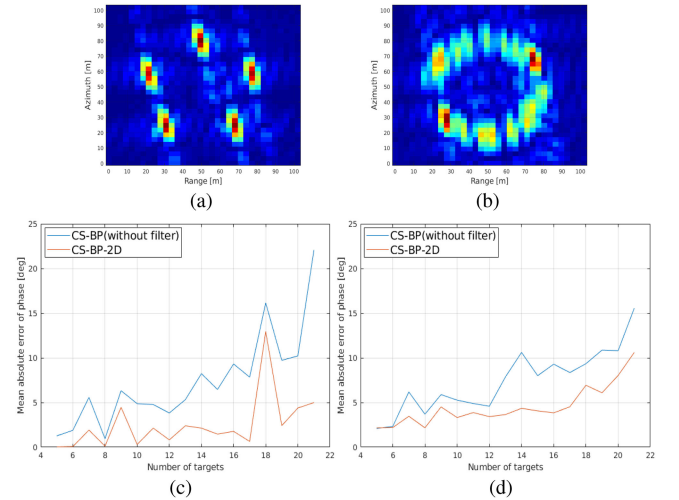

Fig. 13. Experimental results on varying the sparsity level of the scene: (a) SAR image containing 5 strong scatterers (b) SAR image containing 21 strong scatterers (c) MAE on full data, and (d) MAE using 50% of the raw data.

The phase errors were evaluated relative to the SAR image focused by BP and with SNR= ∞. Next, we have varied the sparsity degree of the scene (100×100 m) by changing the number of targets from 5 to 21. The targets are laying along a circular pattern. The first and the last focused SAR images are shown in Fig. 13(a) and (b). We have computed the MAE of the phase for the CS-BP (without filter) and CS-BP-2D using BP outcomes as references. The results are shown in Fig. 13. The experiment was executed using the full data and with 50%

TABLE III
STANDARD DEVIATIONS FOR MAGNITUDE AND PHASE OBTAINED IN THE GRID MISMATCH EXPERIMENT

	% of used data	BP	CS-BP (without filter)	CS-BP-2D
σ phase [deg]	100%	0.3524	0.8375	**0.3524**
σ magnitude		0.0036	0.0217	**0.0132**
σ phase [deg]	50%	0.6806	5.2525	**2.3329**
σ magnitude		0.0033	0.0093	**0.0056**

TABLE IV
EXPERIMENTAL PARAMETERS FOR REAL-WORLD DATA

Parameter	Value
Carrier frequency	5.405 GHz
Bandwidth / Range resolution	47.46 MHz / 3.16 m
Sampling frequency	54.596 MHz (IQ)
Window	Hamming
Aperture length / Azimuth resolution (monostatic)	1045.8 m / 22.979m
Pulse Repetition Frequency	1.4516 kHz
Acquisition mode	TOPS
Range	∼866 km

randomly under-sampled data. For the test that involved discarded data, the MAE was obtained by averaging 10 Monte Carlo simulations. For the last experiment on simulated data, we have tested the behavior of CS-BP-2D with respect to grid mismatch. We have considered a monostatic configuration and a sparse region of interest (100×100 m) containing three-point scatterers with normalized magnitudes of 1.0, 0.75, and 0.4, respectively. The grid cell spacing was 3 m. Initially, the scatterers were located exactly on the grid points. Then, the imaging grid has been randomly shifted over 100 iterations. The maximum shift relative to the initial position was ≈ 0.8 m. We have evaluated the performance of BP, CS-BP (without PSF-based filter), and CS-BP-2D in terms of phase and amplitude variance (σ) over 1000 iterations. The results are synthesized in Table III. CS-BP-2D achieves a better phase estimate than classic CS-BP. In addition, the reconstruction of the amplitude is less influenced by the grid mismatch. The improvement is determined by the PSF-based filter which discards the residual points reconstructed by conventional CS-BP. In this way, CS-BP-2D accounts for the grid mismatch errors.

B. Real-World Data

The raw data for the monostatic configuration tests was extracted from Sentinel-1 L0 products by decoding them compliant to the "Sentinel-1 SAR Space Packet Protocol Data Unit" specification [43]. The bistatic SAR setup includes Sentinel-1B as transmitter of opportunity for the COBIS ground-based receiver [44]. COBIS is located in a fixed position, on the roof of the central building of University "Politehnica of Bucharest (UPB). A detailed description of the acquisition process is given in [44].

For the monostatic setup, raw data consists of 200 azimuth measurements with 24140 range samples, selected from a single burst. As a consequence, the azimuth resolution is worse than the Sentinel 1 full azimuth resolution in TOPS mode. The data for the bistatic scenario consists of 300 range profiles of 50 000 samples each. All SAR images to be shown are focused on geocoded grids. Other parameters of the experiments are synthesized in Table IV.

1) Monostatic Case: The goal of our investigation is to show that the proposed framework preserves image readability in real-world urban sparse scenarios. Besides, we also evaluate the phase reconstruction accuracy given the increasing interest in monitoring civil engineering structures with SAR differential interferometry. We provide imaging results for two regions: Palace of Parliament (PP) and Vulcan Value Center (VVC), Bucharest, Romania. In Fig. 14, the BP and the CS-BP-2D
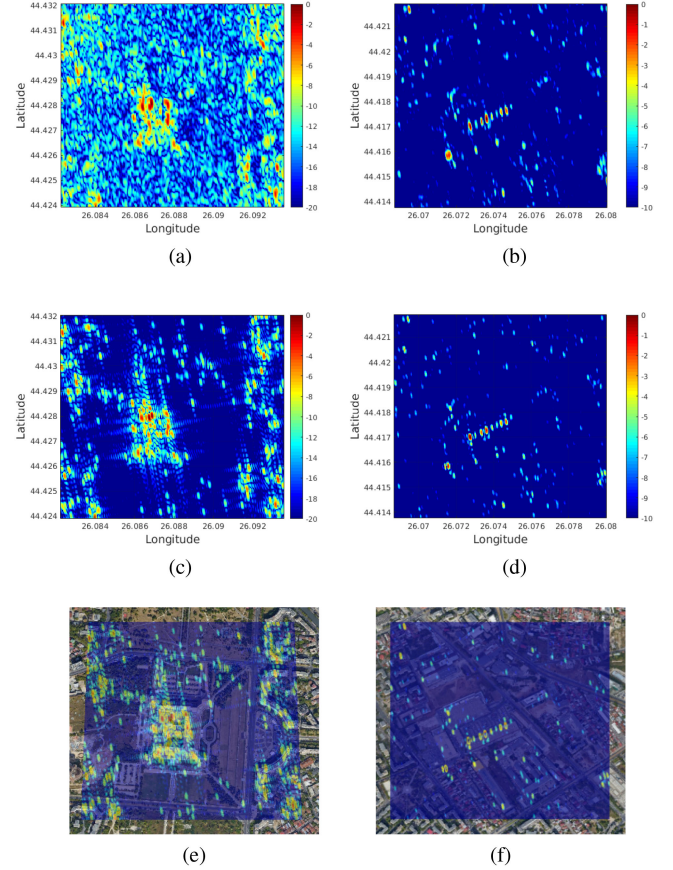

Fig. 14. Monostatic SAR images of Palace of Parliament and Vulcan Value Center, Bucharest: (a) BP SAR image of PP, (b) BP SAR image of VVC, (c) CS-BP-2D SAR image of PP, (d) CS-BP-2D SAR image of VVC. In (e) and (f) the CS-BP-2D outcomes overlay optical images from Google Earth.

outcomes are displayed. Both SAR images cover equal square areas of 900×900 m. The SAR images are focused on geocoded grids having a mean altitude of 100 m. The grid cell, i.e., pixel size is 1 m. Fig. 14(a) and (b) illustrates BP imaging results, whereas in Fig. 14(c) and (d), the CS-BP-2D SAR images are shown. Structural features conservation is validated in Fig. 14(e) and (f), where SAR images overlay Google Earth optical images. For CS-BP-2D, 23% of the raw data were discarded.

In the following, for a region of 200×240 m containing VVC, experiments testing super-resolution potential and phase component conservation are conducted. The chosen area is representative because it contains point-like targets, and the hypothesis of spatial sparsity holds. Ground-truth measurements
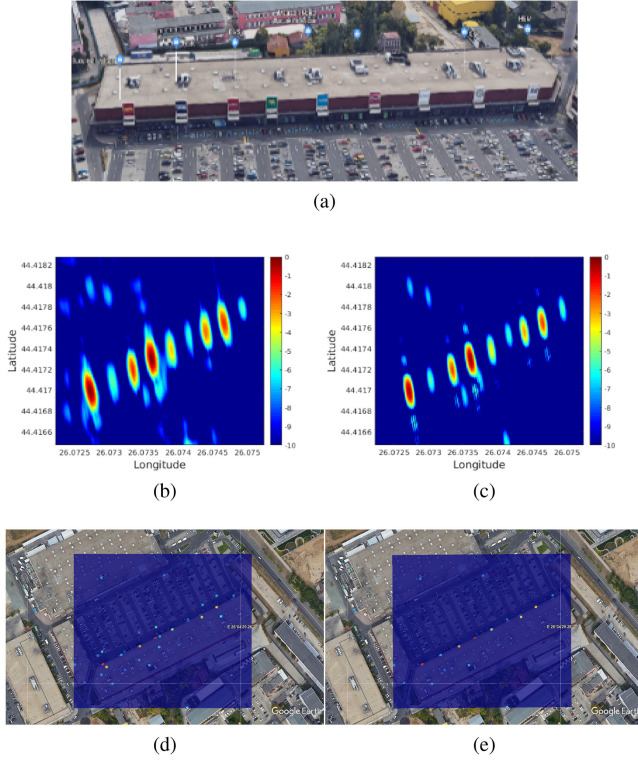
(a)

(b)   (c)

(d)   (e)

Fig. 15. Enlarged area incorporating point reflectors from VVC: (a) Optical image of the scene, (b) BP outcome [dB], (c) CS-BP-2D SAR image (with PSF) [dB].In (d) and (e) the raw CS-BP (without filter) outcome and the raw SAR image obtained by CS-BP-2D overlaying Google Earth optical images are displayed. After the PSF-based filter is applied, the remaining points match the logo panels locations.

with laser telemeter were taken to certify that the echoed signal corresponds to the commercial brands' logo panels shown in Fig. 15(a). The outcome provided by the recovery algorithm consists of isolated reconstructed points, i.e., a superposition of Delta functions, e.g., Fig. 15(d) raw result obtained by CS-BP (without filter) and Fig. 15(e)-CS-BP-2D. For a better visualization, these results are convoluted with a modified system PSF, [45] e.g., Fig. 15(c).

$$\sigma_{\mathrm{CS}}^2 = \sum_{i=1}^{K} \frac{((\angle \boldsymbol{I}_{\mathrm{BP}} - \angle \boldsymbol{I}_{\mathrm{CS}}) - m)^2}{K - 1}. \tag{14}$$

The quality of the reconstructed image varies with the amount of discarded data and the SNR. Therefore, to demonstrate the superiority of the proposed imaging framework, a Monte Carlo (MC) simulation with 100 trials has been run on real data. For each of the trials, a different set of randomly selected samples representing 77% from the raw data was used. We chose the pixel spacing of the generated SAR images to be 3m. The coarse level of sparsity was fixed to $K = 25$.

$$m = \sum_{i=1}^{K} \frac{\angle \boldsymbol{I}_{\mathrm{BP}} - \angle \boldsymbol{I}_{\mathrm{CS}}}{K}. \tag{15}$$

The relative phase error variance was computed using (11). The mean error m was calculated using (15). For CS-BP (without filter) approach, a mean $m = 0.1026$ [rad] and variance of
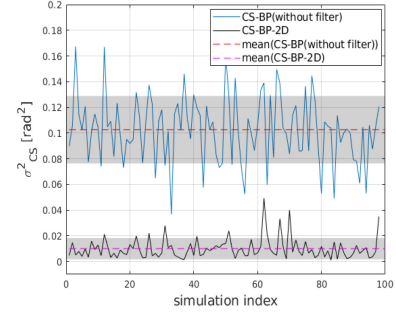

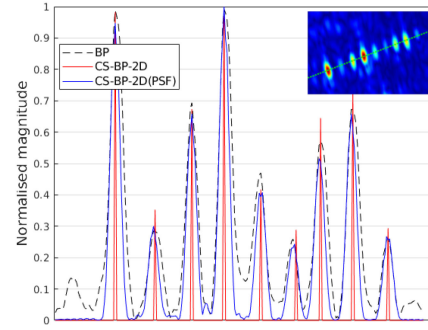Fig. 16. Monte Carlo simulation results.

Fig. 17. Normalized sections on SAR images.

$\sigma^2 = 0.0262 [\mathrm{rad}^2]$ were obtained, whereas CS-BP-2D performances include a mean $m = 0.01$ [rad] and a variance $\sigma^2 = 0.0083$ [rad^2].

In Fig. 16, the phase reconstruction performance of the proposed algorithm is depicted by mean and variance computed for every MC trial. Not only the spread of σ_{CS}, graphically marked as gray transparent bands, which show great improvement of CS-BP-2D in comparison with classic OMP, but also the average variance of the proposed methodology is 10 times smaller than the CS-BP(without filter) framework.

Further, the main lobe narrowing and side-lobe reduction produced by BP-CS-2D are emphasized in Fig. 17, where a section over the magnitude of the SAR images in Fig. 15 is taken. As marked in the upper-right corner of the figure, the chosen section crosses nine-strong scatterers. CS-BP-2D benefits from the employment of a greedy solver. The dominant scatterers are highlighted, therefore the overall perception of the reconstructed image is improved. This feature can be noticed in Fig. 18.

Six rectangular patches (1000×1000 m) were used to create the final CS-BP-2D result. They are delimited by dashed lines in Fig. 18(b). The middle-left patch contains the PP, while the VVC is imaged in the bottom-right chip. Since the postprocessing filter is applied after the OMP raw results are assembled, the problem of the points corresponding to the same scatterer but included in both patches is solved.

2) Bistatic Case: In this experiment, Sentinel-1B is transmitter of opportunity for COBIS ground-based receiver, [44]. The acquisition geometry is sketched in Fig. 1. The receiver antenna is mounted on the top of the UPB central building and its direction of maximum radiation is oriented towards east–south–east parallel to the ground. Therefore, spatial sparsity is guaranteed
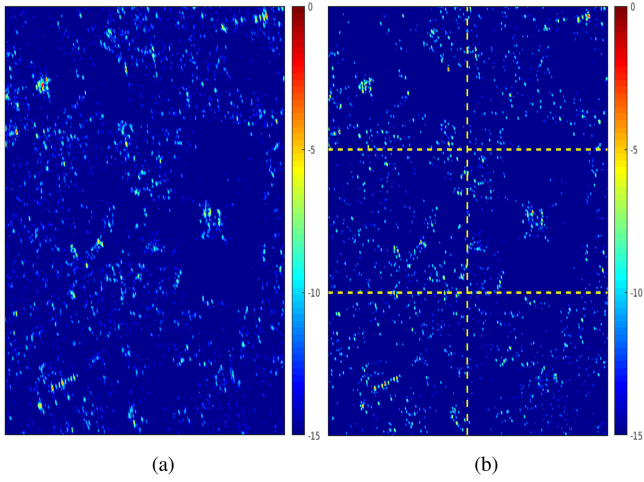
Fig. 18. Normalized imaging results (in dB) on extended scene in monostatic configuration for (a) BP and (b) CS-BP-2D obtained by patch-based workflow (modified PSF included).
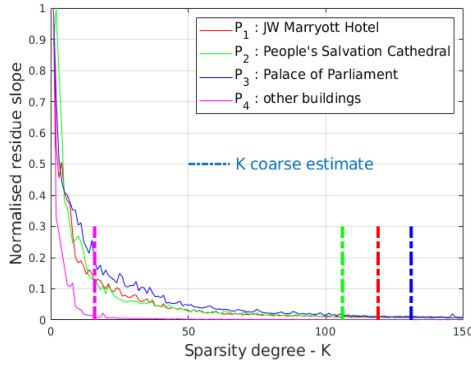

Fig. 19. K coarse estimation for bistatic data.

Fig. 20. Imaging results on bistatic real-world data. (a) BP SAR image, (b) CS-BP(without filter) SAR image, and (c) CS-BP-2D SAR image.
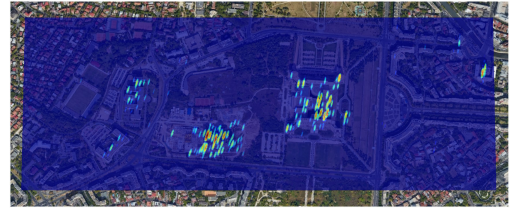
Fig. 21. CS-BP-2D outcome applied on bistatic real world data overlaying Google Earth optical image.
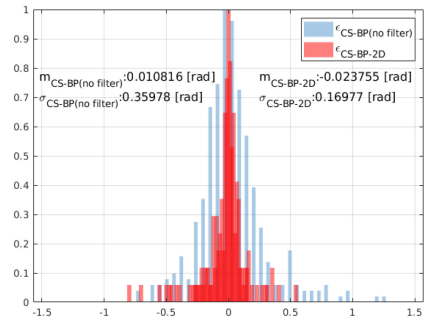
Fig. 22. Relative phase error histograms (ϵ) corresponding to the bistatic setup comparing CS-BP(without filter) and CS-BP-2D.

by the few targets (tall buildings) included in the main beam: Palace of Parliament, People's Salvation Cathedral, JW Marriott Bucharest Grand Hotel, and Ministry of Defense Main Building.

Each of the four reconstructed chips assumed a different coarse sparsity degree $K = \{119, 106, 131, 16\}$. As can be observed in Fig. 19, these values were obtained by using a threshold of 0.01 on the normalized residue energy slope. The analyzed area is 2500×800 m. The CS-BP-2D SAR image overlaying Google Earth optical image representing the area of interest is sketched in Fig. 21. Four patches of 500×800 m were stacked to produce the outcome of CS-BP-2D [see Fig. 20(c)].

The amplitudes of the bistatic SAR images obtained by different approaches are displayed in Fig. 20. Even though the CS-BP outcome Fig. 20(b) has a greater degree of similarity to BP SAR image in Fig. 20 than CS-BP-2D result Fig. 20, it contains many artifacts.

The phase reconstruction accuracy of the proposed processing flow is compared to the one obtained by the regular CS-BP workflow Fig. 22. The reconstruction process used only 75% from the raw data samples.

The blue and red normalized histograms in Fig. 22 show the error of the phase relative to the BP imaging outcome. The standard deviation of the relative phase error obtained by
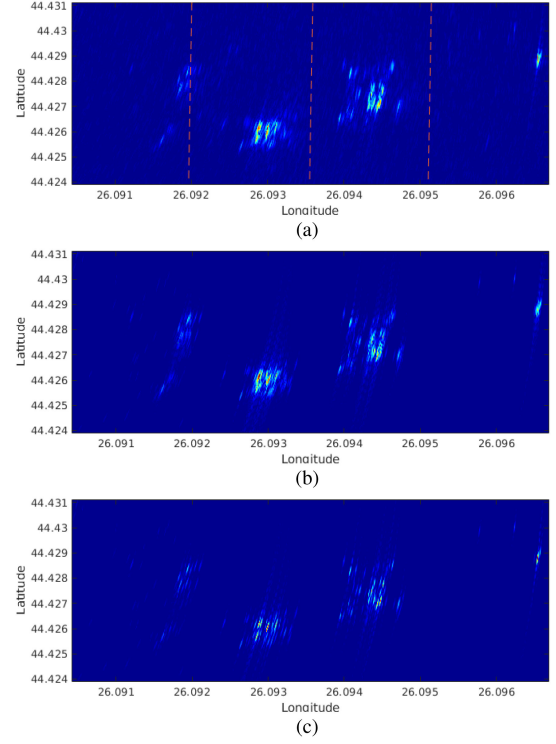
CS-BP-2D is more than two times smaller than the one produced by classic CS-BP reconstruction.

VI. CONCLUSION

In this article, a BP-CS SAR focusing algorithm (for a user-defined grid) was proposed. Both benefits inherited from BP

and matching pursuit are exploited. The BP sparsifying basis was designed together with a PSF-based artifact rejection filter. The obtained SAR images are focused on geo-referenced grids having, in principle, no need for coregistration in future interferometric applications. The imaging results using simulated data and real-world monostatic and bistatic SAR data were presented and interpreted. It was shown that using the proposed processing flow not only the number of recorded samples may be decreased but also the resulted images had been enhanced by reducing the clutter and having the potential of super-resolution. Because of the *STM* intrinsic structure, the CS-BP-2D outcome is similar to that of a deconvolution technique thus to increases SAR image readability synthetic PSF has been included. The proposed CS-BP-2D algorithm successfully reconstructs of both amplitude and phase components of the complex-valued SAR image. The use of the expected PSF as filter kernel proved that the recovered phase is more reliable for interferometric applications than the one recovered by conventional OMP. The sparsity level K relaxation together with postprocessing filter improves weak target detection and SAR image readability as compared to the standard CS-BP (without filter) workflow.

REFERENCES

[1] M. T. Alonso, P. Lopez-Dekker, and J. J. Mallorqui, "A novel strategy for radar imaging based on compressive sensing," *IEEE Trans. Geosci. Remote Sens.*, vol. 48, no. 12, pp. 4285–4295, Dec. 2010.

[2] R. Baraniuk and P. Steeghs, "Compressive radar imaging," in *Proc. IEEE radar conf.*, 2007, pp. 128–133.

[3] X. Dong and Y. Zhang, "A novel compressive sensing algorithm for SAR imaging," *IEEE J. Sel. Top. Appl. Earth Observ. Remote Sens.*, vol. 7, no. 2, pp. 708–720, Feb. 2014.

[4] J. Fang, Z. Xu, B. Zhang, W. Hong, and Y. Wu, "Fast compressed sensing SAR imaging based on approximated observation," *IEEE J. Sel. Topics Appl. Earth Observ. Remote Sens.*, vol. 7, no. 1, pp. 352–363, Jan. 2014.

[5] S. Camlica, A. C. Gurbuz, and O. Arikan, "Autofocused spotlight SAR image reconstruction of off-grid sparse scenes," *IEEE Trans. Aerosp. Electron. Syst.*, vol. 53, no. 4, pp. 1880–1892, Aug. 2017.

[6] R. Karlina and M. Sato, "Compressive sensing applied to imaging by ground-based polarimetric SAR," in *Proc. IEEE Int. Geosci. Remote Sens. Symp.*, 2011, pp. 2861–2864.

[7] M. Pieraccini, N. Rojhani, and L. Miccinesi, "Compressive sensing for ground based synthetic aperture radar," *Remote Sens.*, vol. 10, no. 12, 2018, Art. no. 1960.

[8] B. Hou, G. Zhang, Z. Li, and L. Jiao, "Sparse coding-inspired high-resolution ISAR imaging using multistage compressive sensing," *IEEE Trans. Aerosp. Electron. Syst.*, vol. 53, no. 1, pp. 26–40, Feb. 2017.

[9] E. Giusti, D. Cataldo, A. Bacci, S. Tomei, and M. Martorella, "ISAR image resolution enhancement: Compressive sensing versus state-of-the-art super-resolution techniques," *IEEE Trans. Aerosp. Electron. Syst.*, vol. 54, no. 4, pp. 1983–1997, Aug. 2018.

[10] M.-S. Kang, S.-H. Lee, K.-T. Kim, and J.-H. Bae, "Bistatic ISAR imaging and scaling of highly maneuvering target with complex motion via compressive sensing," *IEEE Trans. Aerosp. Electron. Syst.*, vol. 54, no. 6, pp. 2809–2826, Dec. 2018.

[11] C. Hu, L. Wang, and O. Loffeld, "Inverse synthetic aperture radar imaging exploiting dictionary learning," in *Proc. IEEE Radar Conf.*, 2018, pp. 1084–1088.

[12] M. C. Shastry, R. M. Narayanan, and M. Rangaswamy, "Sparsity-based signal processing for noise radar imaging," *IEEE Trans. Aerosp. Electron. Syst.*, vol. 51, no. 1, pp. 314–325, Jan. 2015.

[13] X. X. Zhu and R. Bamler, "Super-resolution power and robustness of compressive sensing for spectral estimation with application to spaceborne tomographic SAR," *IEEE Trans. Geosci. Remote Sens.*, vol. 50, no. 1, pp. 247–258, Jan. 2012.

[14] Y. Shi, X. x. Zhu, and R. Bamler, "Nonlocal compressive sensing-based SAR tomography," *IEEE Trans. Geosci. Remote Sens.*, vol. 57, no. 5, pp. 3015–3024, May 2019.

[15] R. Giordano, P. Guccione, G. Cifarelli, L. Mascolo, and G. Nico, "Focusing SAR images by compressive sensing: Study of interferometric properties," in *Proc. IEEE Int. Geosci. Remote Sens. Symp.*, 2015, pp. 5352–5355.

[16] W. Feng, G. Nico, and M. Sato, "GB-SAR interferometry based on dimension-reduced compressive sensing and multiple measurement vectors model," *IEEE Geosci. Remote Sens. Lett.*, vol. 16, no. 1, pp. 70–74, Jan. 2019.

[17] H. Yang, C. Chen, S. Chen, F. Xi, and Z. Liu, "Non-common band SAR interferometry via compressive sensing," *IEEE Trans. Geosci. Remote Sens.*, vol. 58, no. 6, pp. 4436–4453, 2020, doi: 10.1109/TGRS.2020.2964701.

[18] V. H. Tang, A. Bouzerdoum, and S. L. Phung, "Multipolarization through-wall radar imaging using low-rank and jointly-sparse representations," *IEEE Trans. Image Process.*, vol. 27, no. 4, pp. 1763–1776, Apr. 2018.

[19] A. H. Muqaibel and A. A. Albeladi, "Dynamic joint reconstruction of walls and targets in through-the-wall radar imaging," *IEEE Access*, vol. 7, pp. 134028–134035, Sep. 2019.

[20] R. G. Baraniuk, "Compressive sensing [*lecture notes*]," *IEEE Signal Process. Mag.*, vol. 24, no. 4, pp. 118–121, 2007.

[21] A. De Maio, Y. C. Eldar, and A. M. Haimovich, *Compressed Sensing in Radar Signal Processing*. Cambridge, U.K.: Cambridge Univ. Press, 2020.

[22] W. Pu, Y. Huang, J. Wu, H. Yang, and J. Yang, "Fast compressive sensing-based SAR imaging integrated with motion compensation," *IEEE Access*, vol. 7, pp. 53284–53295, Apr. 2019.

[23] H. Bi, G. Bi, B. Zhang, and W. Hong, "Complex-image-based sparse SAR imaging and its equivalence," *IEEE Trans. Geosci. Remote Sens.*, vol. 56, no. 9, pp. 5006–5014, Sep. 2018.

[24] W. Pu and J. Wu, "OSRANP: A novel way for radar imaging utilizing joint sparsity and low-rankness," *IEEE Trans. Comput. Imag.*, vol. 6, pp. 868–882, May 2020.

[25] C. Zeng, W. Zhu, X. Jia, and L. Yang, "Sparse aperture ISAR imaging method based on joint constraints of sparsity and low rank," *IEEE Trans. Geosci. Remote Sens.*, vol. 59, no. 1, pp. 168–181, Jan. 2021.

[26] J. Yang, T. Jin, and X. Huang, "Compressed sensing radar imaging with magnitude sparse representation," *IEEE Access*, vol. 7, pp. 29722–29733, Mar. 2019.

[27] E. van denBerg and M. P. Friedlander, "SPGL1: A solver for large-scale sparse reconstruction," Dec. 2019. [Online]. Available: https://friedlander.io/spgl1

[28] M. Soumekh, *Synthetic Aperture Radar Signal Processing*, vol. 7. New York, NY, USA: Wiley, 1999.

[29] M. Albuquerque, P. Prats, and R. Scheiber, "Applications of time-domain back-projection SAR processing in the airborne case," in *Proc. 7th Eur. Conf. Synthetic Aperture Radar*, pp. 1–4, 2008.

[30] M. Rodriguez-Cassola, P. Prats-Iraola, G. Krieger, and A. Moreira, "On the use of time-domain SAR focusing in spaceborne SAR missions," in *Proc. IGARSS IEEE Int. Geosci. Remote Sens. Symp.*, 2019, pp. 755–758.

[31] A. Cohen, W. Dahmen, and R. DeVore, "Orthogonal matching pursuit under the restricted isometry property," *Constructive Approximation*, vol. 45, no. 1, pp. 113–127, 2017.

[32] B. D. Rigling and R. L. Moses, "Polar format algorithm for bistatic SAR," *IEEE Trans. Aerosp. Electron. Syst.*, vol. 40, no. 4, pp. 1147–1159, Oct. 2004.

[33] M. Rodriguez-Cassola, P. Prats, G. Krieger, and A. Moreira, "Efficient time-domain image formation with precise topography accommodation for general bistatic SAR configurations," *IEEE Trans. Aerosp. Electron. Syst.*, vol. 47, no. 4, pp. 2949–2966, Oct. 2011.

[34] L. A. Gorham and L. J. Moore, "SAR image formation toolbox for MATLAB," in *Proc. Algorithms Synthetic Aperture Radar Imagery XVII*, vol. 7699, 2010, Art. no. 769906.

[35] J. Romberg, "Sensing by random convolution," in *Proc. 2nd IEEE Int. Workshop Comput. Adv. Multi-Sensor Adaptive Process.*, 2007, pp. 137–140.

[36] E. J. Candès, J. Romberg, and T. Tao, "Robust uncertainty principles: Exact signal reconstruction from highly incomplete frequency information," *IEEE Trans. Information Theory*, vol. 52, no. 2, pp. 489–509, Feb. 2006.

[37] E. J. Candès and M. B. Wakin, "An introduction to compressive sampling," *IEEE Signal Process. Mag.*, vol. 25, no. 2, pp. 21–30, Mar. 2008.

[38] S. F. Cotter, B. D. Rao, K. Engan, and K. Kreutz-Delgado, "Sparse solutions to linear inverse problems with multiple measurement vectors," *IEEE Trans. Signal Process.*, vol. 53, no. 7, pp. 2477–2488, Jul. 2005.

[39] Z. Ben-Haim, Y. C. Eldar, and M. Elad, "Coherence-based performance guarantees for estimating a sparse vector under random noise," *IEEE Trans. Signal Process.*, vol. 58, no. 10, pp. 5030–5043, Oct. 2010.

[40] D. Needell and R. Vershynin, "Signal recovery from incomplete and inaccurate measurements via regularized orthogonal matching pursuit," *IEEE J. Sel. Top. Signal Process.*, vol. 4, no. 2, pp. 310–316, Apr. 2010.

[41] J. Wang, S. Kwon, and B. Shim, "Generalized orthogonal matching pursuit," *IEEE Trans. Signal Process.*, vol. 60, no. 12, pp. 6202–6216, Dec. 2012.

[42] Y. Wang, Y. Y. Tang, and L. Li, "Correntropy matching pursuit with application to robust digit and face recognition," *IEEE Trans. Cybernetics*, vol. 47, no. 6, pp. 1354–1366, Jun. 2017.

[43] H. Flachs, "Sentinel-1 SAR space packet protocol data unit," Tech. Rep. S1-IF-ASD-PL-0007, Airbus DS, 2015.

[44] A. Anghel, R. Cacoveanu, A.-S. Moldovan, B. Rommen, and M. Datcu, "COBIS: Opportunistic C-band bistatic SAR differential interferometry," *IEEE J. Sel. Top. Appl. Earth Observ. Remote Sens.*, vol. 12, no. 10, pp. 3980–3998, Oct. 2019.

[45] A. Dongyang, W. Rui, H. Cheng, and Y. Li, "A sparse SAR imaging method based on multiple measurement vectors model," *Remote Sens.*, vol. 9, no. 297, 2017.

Adrian Focsa (Student Member, IEEE) received the B.S. degree in electronics and telecommunications from the Military Technical Academy, Bucharest, Romania, in 2016, and the M.S. degree in electronics and telecommunications from Politehnica University Politehnica of Bucharest (UPB), Bucharest, Romania in 2018. He is currently working toward the Ph.D. degree in electronics and telecommunications with Politehnica University of Bucharest, Bucharest, Romania.

He joined the CEOSpaceTech Center from UPB in 2015, when he also worked at German Aerospace Center (DLR) during two months of internship. He took part in several national and international research projects. His areas of interest include: synthetic aperture radar, SAR interferometry, compressive sensing, and machine learning.

Andrei Anghel (Senior Member, IEEE) received the Engineering degree (as valedictorian) and the M.S. degree (with the highest grade) in electronic engineering and telecommunications from the Politehnica University Politehnica of Bucharest (UPB), Bucharest, Romania, in 2010 and 2012, respectively and the joint Ph.D. degree in signal, image, speech, and telecommunications from the University of Grenoble Alpes, Grenoble, France, and in electronic engineering and telecommunications (summa cum laude) from the University UPB, Bucharest, Romania in 2015. He received the habilitation degree in electronic engineering, telecommunications, and information technologies from the University Politehnica of Bucharest, Bucharest, Romania, in 2020.

Between 2012 and 2015, he worked as a Doctoral Researcher with Grenoble Image Speech Signal Automatics Laboratory (GIPSA-lab), Grenoble, France. In 2012, he joined the University Politehnica of Bucharest as a Teaching Assistant, where he is currently an Associate Professor with the Telecommunications Department, Faculty of Electronics, Telecommunications and Information Technology. He is the author of more than 50 scientific publications, 2 textbooks, and a book about SAR signal processing for infrastructure monitoring. His current research interests include remote sensing, radar, microwaves, and signal processing.

Dr. Anghel regularly acts as a Reviewer for several IEEE and IET journals. He was the recipient of two gold medals (in 2005 and 2006) at the International Physics Olympiads.

Mihai Datcu (Fellow, IEEE) received the M.S. and Ph.D. degrees in electronics and telecommunications from the University Politehnica of Bucharest (UPB), Bucharest, Romania, in 1978 and 1986, respectively, and the habilitation a Diriger Des Recherches degree in computer science from the University Louis Pasteur, Strasbourg, France, in 1999.

Since 1981, he has been a Professor with the Department of Applied Electronics and Information Engineering, Faculty of Electronics, Telecommunications and Information Technology, UPB. Since 1993, he has been a Scientist with the German Aerospace Center (DLR), Wessling, Germany. His research interests include explainable and physics aware artificial intelligence, smart radar sensors design, and qauntum machine learning with applications in Earth Observation. He has held Visiting Professor appointments with the University of Oviedo, Spain, the University Louis Pasteur and the International Space University, both in Strasbourg, France, University of Siegen, Germany, University of Innsbruck, Austria, University of Alcala, Spain, University Tor Vergata, Rome, Italy, University of Trento, Italy, Unicamp, Campinas, Brazil, China Academy of Science (CAS), Shenyang, China, Universidad Pontificia de Salamanca, campus de Madrid, Spain, University of Camerino, Italy, the Swiss Center for Scientific Computing (CSCS), Manno, Switzerland. From 1992 to 2002, he had an Invited Professor assignment with the Swiss Federal Institute of Technology (ETH Zurich), Switzerland. Since 2001, he had been initiating and leading the Competence Center on Information Extraction and Image Understanding for Earth Observation, Paris Institute of Technology, ParisTech, France, a Collaboration of DLR with the French Space Agency (CNES). He has been a Professor holder of the DLR-CNES Chair with ParisTech. He has initiated the European frame of projects for image information mining (IIM) and is involved in research programs for information extraction, data mining, and knowledge discovery, and data science with the European Space Agency (ESA), NASA, and in a variety of national and European projects. He is the Director of the Research Center for Spatial Information, UPB. He is a Senior Scientist and the Data Intelligence and Knowledge Discovery Research Group Leader with the Remote Sensing Technology Institute, DLR, and delegate in the DLR-ONERA Joint Virtual Center for AI in Aerospace.

Dr. Datcu is member of the ESA Working Group Big Data from Space and Visiting Professor withe ESA's Φ-Lab. He was the recipient the National Order of Merit with the rank of Knight, for outstanding international research results, awarded by the President of Romania, in 2008, and the Romanian Academy Prize Traian Vuia for the development of the SAADI image analysis system and his activity in image processing, in 1987, and of the Chaire d'excellence internationale Blaise Pascal 2017 for international recognition in the field of data science in earth observation. He has served as a Co-organizer for international conferences and workshops and as Guest Editor for a special issues on AI and Big Data of the IEEE and other journals. He is a representative of Romanian in the Earth Observation Program Board (EO-PB).

Stefan-Adrian Toma received the engineering degree in electronics and telecommunications from the Military Technical Academy "Ferdinand I", Bucharest, Romaniain 2004, the M.S. degree in electronics and telecommunications from the "Politehnica" University of Bucharest, Bucharest, Romania, in 2007, and the Ph.D. degree in electronics and telecommunications from the Military Technical Academy "Ferdinand I", Bucharest, Romania, in 2011.

Between 2014 and 2015, he was the recipient of a postdoctoral scholarship from the Military Technical Academy "Ferdinand I", during which he developed algorithms for nonlinearities correction. He is currently an Associate Professor with the Computer Science Department of the Military Technical Academy "Ferdinand I". He collaborates closely with the industry on PSInSAR, machine learning, and radar system development, was involved in more than ten research projects won through national or international competitions and was Project Manager and lead the research teams for three of them.